Available online at www.sciencedirect.com
SCIENCE DIRECT®
Mechanics of Materials 38 (2006) 203–217
MECHANICS OF MATERIALS
www.elsevier.com/locate/mechmat

Micro-mechanical modeling of the inelastic behavior of directionally solidified materials

K. Sai [a], G. Cailletaud [b,*], S. Forest [b]

[a] LGPMM, Ecole Nationale d'Ingénieurs de Sfax, BP W 3038, Tunisia
[b] Centre des Matériaux/UMR 7633, Ecole des Mines de Paris/CNRS, BP 87, 91003 Evry Cedex, France

Received 20 April 2004; received in revised form 7 March 2005

Abstract

Micro-mechanically based constitutive models representing inelastic behavior of directionally solidified (DS) materials are proposed. A finite element (FE) computation used to calibrate the model is first presented. It is compared with a model using a static homogenization scheme (uniform stress throughout the material). These approaches lead to significantly different results. A new model is then proposed with a suitable scale transition rule from the macroscopic level to the grain level. Satisfactory results are obtained for this second model, at the macroscopic level as well as for local responses.

Keywords: Single crystal; Directionally solidified; β-Model; Inelastic behavior; Crystal plasticity

1. Introduction

Directionally solidified (DS) materials are sometimes a good compromise between too expensive single crystals and less resistant polycrystals for structures like turbine blades operating at high temperatures. Nevertheless, despite the importance of these materials, little has been done to develop constitutive models able to describe their overall mechanical properties. DS materials are known for their excellent tensile ductility and their high strength at room temperature as well as at high temperature. The morphology of Directionally Solidified materials is such that the grains are purely columnar (Fig. 1). The morphology exhibits a perfect order in the direction of solidification (the x_3 direction coincides with a $\langle 001 \rangle$ direction of each crystal), and a perfect random character in the normal plane. This must be reflected by the scale transition relation in the framework of a micro–macro modeling. There is a growing interest for this type of application, but the state of the art of the modeling activity concerns only elastic

* Corresponding author. Tel.: +33 1 60 76 30 56; fax: +33 1 60 76 31 50.
E-mail address: Georges.Cailletaud@ensmp.fr (G. Cailletaud).

0167-6636/$ - see front matter © 2005 Elsevier Ltd. All rights reserved.
doi:10.1016/j.mechmat.2005.06.007

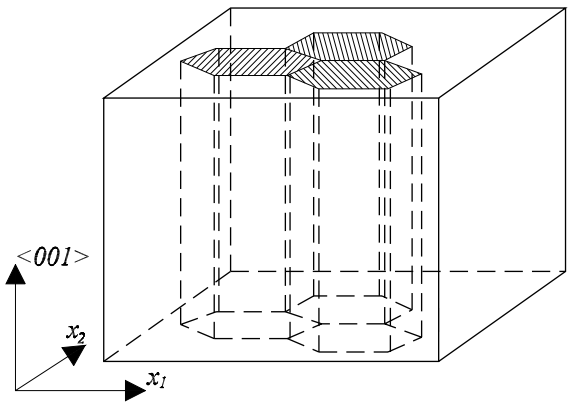

Fig. 1. Columnar morphology of DS grains.

properties (Yaguchi and Busso, 2005). The purpose of the present paper is to propose a strategy for describing this scale transition, using finite element computation to build a reference for the DS aggregate. The local behavior in each grain is supposed to be properly represented by a phenomenological constitutive equation involving nonlinear isotropic and kinematic hardenings. One of the open question is to check if a mean field model is able to predict the global response of the material, even if the description of the intragranular heterogeneities is missing. It should be mentioned that such an attempt was successful in a previous study on a cubic isotropic aggregate (Barbe et al., 2001).

The simplest and most widely used model to predict polycrystal behavior is the Taylor model (Taylor, 1938), where uniform plastic strain in each grain is assumed. Following the self-consistent plasticity model proposed by Hill (1965) many authors revisited the concept of self-consistency (Molinari, 1999) in order to improve polycrystal plasticity models. The aim of this work is to provide a polycrystalline model with a suitable transition rule able to describe DS behavior, having in view target materials like nickel-base directionally solidified superalloys. The model is assessed by means of a finite element (FE) computation in which each grain is represented by a group of elements with a columnar morphology. The overall behavior of the polycrystalline model is compared to the response of a FE model using volume averages of stress and strain. The paper is organized in the following manner: The main lines of constitutive equations for the single crystal model are recalled briefly in the next section. In Section 3 a polycrystalline aggregate model is generated, and computed by the FE technique. The results of this section will provide a database to assess an homogenized polycrystalline model. In that section some statistical analyses of the strain heterogeneity distribution are shown in order to provide a deeper understanding of the local behavior of DS materials. Section 4 is devoted to the comparison between the responses of (i) a "super single crystal" model, (ii) the FE model of the polycrystalline aggregate. In that section an analytical calculation of the yield surface of the "super single crystal" model is presented. In Section 5, a polycrystalline model with an efficient so-called stress concentration procedure is presented. The parameters present in the transition rule are identified from the macroscopic stress–strain curves of the FE model. To assess the reliability of the model, a comparison of local responses is drawn between the polycrystalline model and the FE model. For that purpose, stress–strain curves are compared grain per grain. After checking the response of the proposed model at macroscopic and microscopic levels, a study of the influence of the grain position is performed. An evaluation of the quality of the transition rule with respect to intergranular heterogeneity is also made.

2. Constitutive equations for the single crystal

This section briefly presents the elastoviscoplastic single crystal model used in this work. It has been developed in the framework of crystal plasticity theory (Méric et al., 1991), and widely used, especially for nickel-base superalloys. It is presented here in its small perturbation version, which uses an additive decomposition of the elastic and the viscoplastic strain rates. The so-called resolved shear stress τ^s acting on a particular slip system (s) is given by the relation:

$$\tau^s = \boldsymbol{\sigma}^g : \boldsymbol{m}^s \tag{1}$$

where $\boldsymbol{\sigma}^g$ is the stress tensor in the crystal and $\boldsymbol{m}^s$ is the orientation tensor attributed to the slip system (s):

$$\boldsymbol{m}^s = \frac{1}{2}(\boldsymbol{l}^s \otimes \boldsymbol{n}^s + \boldsymbol{n}^s \otimes \boldsymbol{l}^s) \tag{2}$$

$\boldsymbol{n}^s$ and $\boldsymbol{l}^s$ being the "slip plane" normal vector and the "slip direction" vector in this plane, respectively. The resolved shear stress τ^s can be related to corresponding shear rate $\dot{\gamma}^s$ via a power law expression:

$$\dot{\gamma}^s = \left\langle \frac{|\tau^s - x^s| - r^s}{k} \right\rangle^n \operatorname{sign}(\tau^s - x^s) \tag{3}$$

For each slip system, internal variables are introduced to describe the hardening of the material: isotropic hardening variables r^s and kinematic hardening variables x^s. Viscoplastic flow reaches a rate-independent limit for large values of the parameters n or $1/k$. The nonlinear evolution rule for isotropic hardening involves an interaction matrix $[H]$ which represents self-hardening (diagonal terms) and latent hardening (non-diagonal terms). In the present work, the components H^{rs} are chosen equal to δ^{rs} (Krönecker delta, self-hardening only), since this was shown to be a reasonable approximation for nickel-base superalloys (Méric et al., 1991).

$$r^s = r_0 + Q\sum_r H^{rs}(1 - e^{-bv^r}) \quad \text{with } \dot{v}^r = |\dot{\gamma}^r|. \tag{4}$$

The following form of nonlinear kinematic hardening is adopted:

$$\dot{x}^s = c\dot{\gamma}^s - \dot{v}^s\, dx^s \tag{5}$$

where c and d are material parameters. For the case of FCC materials, plastic deformation in the crystal is the result of slip processes according to 12 octahedral slip systems:

$$\dot{\boldsymbol{\varepsilon}}^{pg} = \sum_{s=1}^{12} \boldsymbol{m}^s \dot{\gamma}^s \tag{6}$$

3. Finite element model

3.1. Computational tools and boundary conditions

The aim of this section is to provide an evaluation of the stress and strain fields in a DS aggregate. For that purpose, an aggregate model is generated and computed by FE technique (Cailletaud et al., 2003). A cube formed by columnar grains is discretised as a regular triangle mesh and the corresponding crystal orientation is attributed to each Gauss point. To generate the mesh corresponding to the microstructure with arbitrary shapes, a 2D Voronoi polyhedra model (Gilbert, 1962) has been used. The mesh includes 39,210 15-nodes prisms with a triangular section and a quadratic nodal interpolation (Fig. 2). The FCC crystal behavior of Section 2 is used with the material parameters shown in Table 1. Different tensile and shear simulations are performed with the following boundary conditions:

- For shear tests, a displacement vector $u_i = \varepsilon_{ij} r_j$ is imposed on the contour (all the nodes of the six faces), where ε is a symmetric tensor and $\vec{r}$ is the position of the considered nodes. The tensor components are:

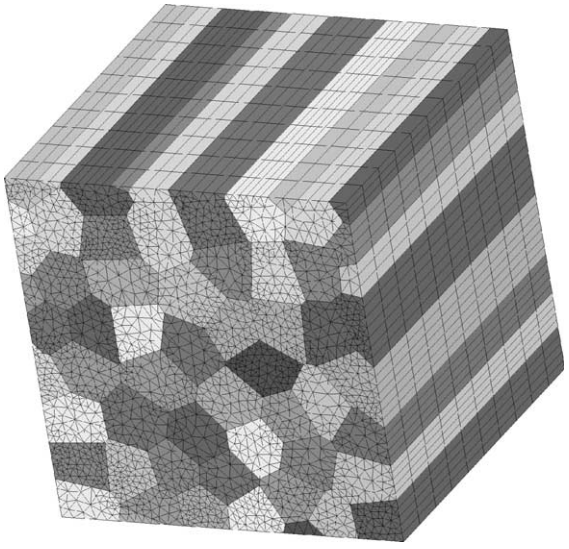

Fig. 2. Mesh of the FE aggregate model.

Table 1
Material parameters

Elasticity		Isotropic hardening			Kinematic hardening	
E (MPa)	v	r_0 (MPa)	Q (MPa)	b	c (MPa)	d
196,000	0.3	111	35	7	1600	40

($\varepsilon_{11} = 0$, $\varepsilon_{22} = 0$, $\varepsilon_{33} = 0$, $\varepsilon_{12} = 1\%$, $\varepsilon_{23} = 0$, $\varepsilon_{13} = 0$) for shear tests in the plane 12,
($\varepsilon_{11} = 0$, $\varepsilon_{22} = 0$, $\varepsilon_{33} = 0$, $\varepsilon_{12} = 0$, $\varepsilon_{23} = 0$, $\varepsilon_{13} = 1\%$) for the shear tests in the plane 13.

- For the tensile tests, four lateral faces are free, whereas an axial displacement is imposed on the two remaining faces.
  For the tensile tests in direction 11: $u_1 = 0$ at the nodes of the face ($x_1 = 0$) and $u_1 = h\varepsilon_{11}$ at the nodes of the opposite face, such that $\varepsilon_{11} = 0.3\%$. For the tensile tests in direction 22: $u_2 = 0$ at the nodes of the face ($x_2 = 0$) and $u_2 = h\varepsilon_{22}$ at the nodes of the opposite face, such that $\varepsilon_{22} = 0.3\%$. For the tensile tests in direction 33: $u_3 = 0$ at the nodes of the bottom ($x_3 = 0$) and $u_3 = h\varepsilon_{33}$ at the nodes of the top, such that $\varepsilon_{33} = 0.5\%$.

Two strategies are tested to generate the set of grain orientations. The first one considers 64 distinct orientations, each of them being generated by rotation around the last Euler angle φ. From now on, this model will be called FE-64-64. In this notation, the first number specifies the number of grains whereas the second number specifies the number of distinct orientations. The second aggregate model considered by FE technique is called FE-64-8. In this aggregate, 8 different orientations are considered. Each orientation is attributed to 8 column-like randomly distributed grains.

3.2. Results of the FE computations

Fig. 3 shows typical contour plots for a tensile test in direction 11 and for a shear test in the plane 13. The von Mises contour plots show a rather small variation of stress field. For this reason, it is reasonable to begin with a static model in which a uniform stress throughout the material is considered. Three kinds of results can be deduced from the FE computations:

(i) The stress–strain curves produced by the global volume average. These results can be obtained by either FE-64-64 or FE-64-8 simulations.
(ii) The volume average on each individual grain which can be obtained by FE-64-64 and FE-64-8 simulations.
(iii) The volume average in each phase (i.e. each set of grains belonging to the same crystallographic orientation class). These results are provided by the FE-64-8 computations.

3.3. Statistical analysis

The FE analyses provide also local stress and strain values inside the grains. These values are important for subsequent damage and lifetime assessment. The stress and strain data generated using the FE simulations are analyzed using statistical techniques in order to study their distribution characteristics in a way similar to (Sarma and Dawson, 1995). The FE aggregate of FE-64-8 model is subjected to shear loading in the plane 13 with four levels of average strain as summarized in Table 2.

The deformation data generated using the finite element simulations where analysed using statistical techniques in order to study their distribution characteristics. Fig. 4 shows the histogram of the ε_{13} component in the volume. A Gaussian distribution function is also plotted as a reference. This demonstrates that the computed distribution is generally not Gaussian. A frequency histogram (Fig. 5) is also plotted for each average strain level and for each last Euler angle φ. The abscissa of each histogram represents the local strain level at Gauss points, and the ordinate the frequency function. These histograms have led to the following remarks:

- As shown in Fig. 5a, most of the histograms are bell-shaped curves. Indeed they are almost symmetric with respect to their mean value. However the peak is always higher than the peak of the respective normal distribution. In such cases, the kurtosis parameter is used to measure the degree of peakedness of a distribution. The kurtosis factor of a distribution is defined as:

$$k = \frac{E((x-\mu)^4)}{\sigma^4} \tag{7}$$

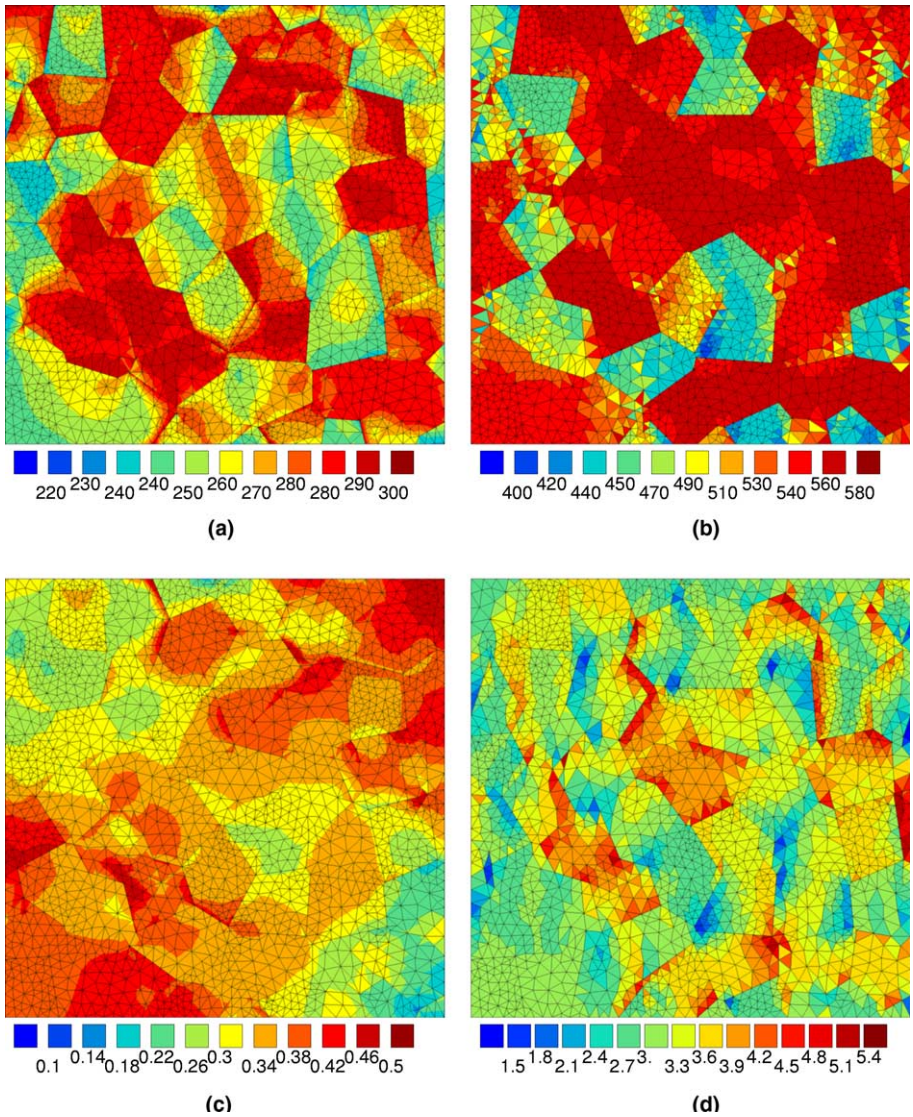

Fig. 3. Contour plot in the FE aggregate: (a) tensile test 11, von Mises stress (MPa), (b) shear test 13, von Mises stress (MPa), (c) tensile test 11, cumulative inelastic strain (%), (d) shear test 13, cumulative inelastic strain (%).

Table 2
Values of the average strain chosen for performing statistical analyses

$\langle\varepsilon_{13}\rangle$	0.195%	0.413%	0.588%	0.755%

where σ is the standard deviation, μ is the mean of x and $E(t)$ denotes the expected value of t. Note that the kurtosis of a normal distribution is 3. Fig. 5b gives for different loading levels kurtosis as function of the angle φ. It appears that they are non-normal distributions.

- Each distribution is characterized by its mean value and its standard deviation. The mean value is almost equal to the corresponding average strain. Fig. 5c shows that the spread (or the dispersion) increases with the loading level. In

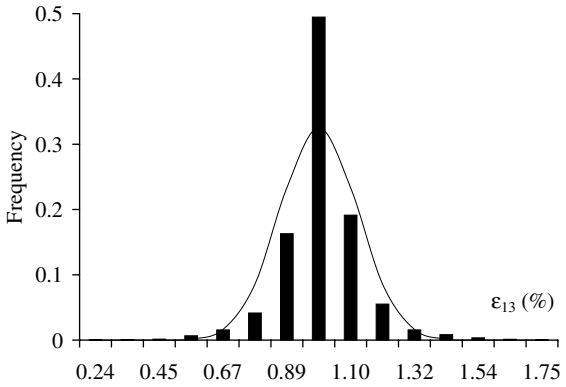

Fig. 4. Histogram and comparison with Gaussian distribution.

the present case, the values of the standard deviations are respectively equal to 0.1335, 0.379, 0.629 and 0.78.

- For some particular angles, the shape of the histogram indicates a multimodal distribution for low as well as for high average strain levels (Fig. 5d).

4. Super single crystal/static model

4.1. Constitutive equations

As a first approximation, it is considered here that internal stresses remain low even during viscoplastic flow. This idea is also supported by the fact that all the grains have already a common axis. Using this simple static assumption and uniform elasticity, a uniform stress field is postulated in the whole aggregate, and the stress concentration

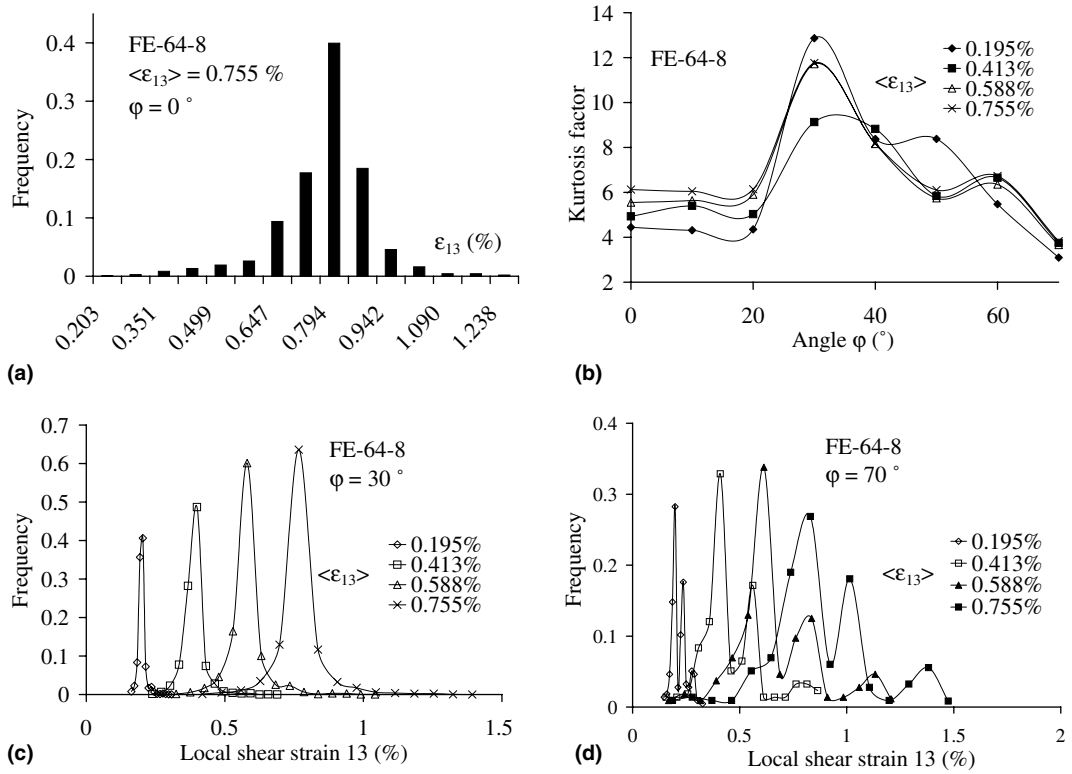

Fig. 5. Statistical analysis for the strain controlled shear test 13. (a) Distribution of local shear strain with fixed angle and fixed average of overall strain. (b) Kurtosis factors for different angles and different loading levels. (c) Spread evolution of the sample with loading with a fixed angle. (d) Example of multimodal histograms for different loading levels with a fixed angle.

procedure is reduced to the equality between the macroscopic stress and the stress in the grain:

$$\boldsymbol{\sigma}^{g} = \boldsymbol{\sigma} \tag{8}$$

The resulting aggregate is like a "super single crystal", or a single crystal having a collection of all the slip systems present in all the grains, since the same stress level is applied to each of them. Once the constitutive behavior of a single crystal is specified, one has to find the overall behavior of an aggregate consisting of columnar oriented grains. The plastic strain of the representative volume element (RVE) is the volume average over all grains:

$$\dot{\varepsilon}^{p} = \overline{\dot{\varepsilon}^{pg}} \tag{9}$$

The additive strain decomposition and Hooke's law give:

$$\varepsilon = \varepsilon^{e} + \varepsilon^{p}, \quad \boldsymbol{\sigma} = \boldsymbol{C} : \varepsilon^{e} \tag{10}$$

where $\boldsymbol{C}$ is the fourth-rank tensor of elastic moduli.

4.2. Analytic calculation of the DS yield surface

Plotting the yield surface is a first solution to have an estimation of the anisotropy of the DS aggregate. In this section, a perfect DS material is considered: All grains have a $\langle 0\,0\,1\rangle$ axis parallel to direction x_3. Let us call it [0 0 1]. A uniform distribution is then assumed for the crystal axis [1 0 0] of the grains. All the axes $\langle 0\,0\,1\rangle$ are the same, they are in the x_3 direction of the aggregate referential, so that axes $\langle 100\rangle$ for instance can take any direction in the x_1–x_2 plane. The resulting yield surfaces will look like Tresca's criterion in a subspace involving x_1 and x_2 axes, but will keep a single crystal character if the axis x_3 is involved. As an illustration, computations are made for a FCC material presenting octahedral slip only. The initial resolved shear stress is 100 MPa. (R_0) is the crystal frame [1 0 0] [0 1 0] [0 0 1], and (R) is the coordinate frame associated with the representative volume element. The transformation between (R_0) and (R) is limited to a single rotation of angle φ around the axis x_3.

Four different stress tensors are considered, in order to illustrate the yield surface for biaxial tension and tension-shear for directions involving x_3 or not:

$$\boldsymbol{\sigma}^{1} = \begin{pmatrix} \sigma_{11} & 0 & 0 \\ 0 & \sigma_{22} & 0 \\ 0 & 0 & 0 \end{pmatrix}, \quad \boldsymbol{\sigma}^{2} = \begin{pmatrix} \sigma_{11} & 0 & 0 \\ 0 & 0 & 0 \\ 0 & 0 & \sigma_{33} \end{pmatrix},$$

$$\boldsymbol{\sigma}^{3} = \begin{pmatrix} 0 & 0 & \sigma_{13} \\ 0 & 0 & 0 \\ \sigma_{13} & 0 & \sigma_{33} \end{pmatrix}, \quad \boldsymbol{\sigma}^{4} = \begin{pmatrix} \sigma_{11} & \sigma_{12} & 0 \\ \sigma_{12} & 0 & 0 \\ 0 & 0 & 0 \end{pmatrix}$$

The components of the four tensors in the crystal frame R_0 are given in Table 3. Accordingly, the 12 resolved stresses of the FCC slip systems are expressed in Tables 4–7. The generic form of these resolved stresses corresponds to a straight line:

$$\tau^{g} = A(\varphi)\sigma_1 + B(\varphi)\sigma_2 \tag{11}$$

where σ_1 and σ_2 are the non-zero components of the considered stress tensor. The inner envelope (which characterizes the yield surface) of this family of straight lines can be obtained (Fig. 6) by introducing a second family of straight lines expressed in polar form:

$$\sigma_1 = \rho(\theta)\cos\theta \quad \text{and} \quad \sigma_2 = \rho(\theta)\sin\theta \tag{12}$$

The polar radius ρ is obtained by replacing σ_1 and σ_2 of Eq. (12) in Eq. (11):

$$\rho(\theta,\varphi) = \frac{\tau^{g}}{A(\varphi)\cos\theta + B(\varphi)\sin\theta} \tag{13}$$

The yield surface is obtained when the polar radius is minimum. Accordingly, the partial derivative of $\rho(\theta,\varphi)$ with respect to φtreating θ as constant must be equal to zero:

Table 3
Transformation of stress tensors

$$\boldsymbol{\sigma}^{1} = \begin{pmatrix} \sigma_{11}\cos^2\varphi + \sigma_{22}\sin^2\varphi & (\sigma_{11}-\sigma_{22})\sin\varphi\cos\varphi & 0 \\ (\sigma_{11}-\sigma_{22})\sin\varphi\cos\varphi & \sigma_{11}\sin^2\varphi + \sigma_{22}\cos^2\varphi & 0 \\ 0 & 0 & 0 \end{pmatrix}$$

$$\boldsymbol{\sigma}^{2} = \begin{pmatrix} \sigma_{11}\cos^2\varphi & \sigma_{11}\sin\varphi\cos\varphi & 0 \\ \sigma_{11}\sin\varphi\cos\varphi & \sigma_{11}\sin^2\varphi & 0 \\ 0 & 0 & \sigma_{33} \end{pmatrix}$$

$$\boldsymbol{\sigma}^{3} = \begin{pmatrix} 0 & 0 & \sigma_{13}\cos\varphi \\ 0 & 0 & \sigma_{13}\sin\varphi \\ \sigma_{13}\cos\varphi & \sigma_{13}\sin\varphi & \sigma_{33} \end{pmatrix}$$

$$\boldsymbol{\sigma}^{4} = \begin{pmatrix} \sigma_{11}\cos^2\varphi - \sigma_{12}\sin 2\varphi & 0.5\sigma_{11}\sin 2\varphi + \sigma_{12}\cos 2\varphi & 0 \\ 0.5\sigma_{11}\sin 2\varphi + \sigma_{12}\cos 2\varphi & \sigma_{11}\sin^2\varphi + \sigma_{12}\sin 2\varphi & 0 \\ 0 & 0 & 0 \end{pmatrix}$$

Table 4
Resolved shear stresses for the slip systems in the space $\sigma_{11}\sigma_{22}$

$\sqrt{6}\tau_1 = (-\cos^2\varphi - \sin\varphi\cos\varphi)\sigma_{11} - (\sin^2\varphi - \sin\varphi\cos\varphi)\sigma_{11}$
$\sqrt{6}\tau_2 = (-\sin^2\varphi - \sin\varphi\cos\varphi)\sigma_{11} - (\cos^2\varphi - \sin\varphi\cos\varphi)\sigma_{22}$
$\sqrt{6}\tau_3 = \cos 2\varphi(\sigma_{22} - \sigma_{22})$
$\sqrt{6}\tau_4 = (-\cos^2\varphi + \sin\varphi\cos\varphi)\sigma_{11} - (\sin^2\varphi + \sin\varphi\cos\varphi)\sigma_{22}$
$\sqrt{6}\tau_5 = (-\sin^2\varphi + \sin\varphi\cos\varphi)\sigma_{11} - (\cos^2\varphi + \sin\varphi\cos\varphi)\sigma_{22}$
$\sqrt{6}\tau_6 = -\cos 2\varphi(\sigma_{22} - \sigma_{11})$
$\sqrt{6}\tau_7 = (-\sin^2\varphi + \sin\varphi\cos\varphi)\sigma_{11} - (\cos^2\varphi + \sin\varphi\cos\varphi)\sigma_{22}$
$\sqrt{6}\tau_8 = \cos 2\varphi - (\sigma_{22} - \sigma_{11})$
$\sqrt{6}\tau_9 = (-\cos^2\varphi + \sin\varphi\cos\varphi)\sigma_{11} - (\sin^2\varphi + \sin\varphi\cos\varphi)\sigma_{22}$
$\sqrt{6}\tau_{10} = \cos 2\varphi(\sigma_{22} - \sigma_{11})$
$\sqrt{6}\tau_{11} = (\cos^2\varphi + \sin\varphi\cos\varphi)\sigma_{11} + (\sin^2\varphi - \sin\varphi\cos\varphi)\sigma_{22}$
$\sqrt{6}\tau_{12} = (\sin^2\varphi + \sin\varphi\cos\varphi)\sigma_{11} + (\cos^2\varphi - \sin\varphi\cos\varphi)\sigma_{22}$

Table 5
Resolved shear stresses for the slip systems in the space $\sigma_{11}\sigma_{33}$

$\sqrt{6}\tau_1 = (-\cos^2\varphi - \sin\varphi\cos\varphi)\sigma_{11} + \sigma_{33}$
$\sqrt{6}\tau_2 = (-\sin^2\varphi - \sin\varphi\cos\varphi)\sigma_{11} + \sigma_{33}$
$\sqrt{6}\tau_3 = -\sigma_{11}\cos 2\varphi$
$\sqrt{6}\tau_4 = (-\cos^2\varphi + \sin\varphi\cos\varphi)\sigma_{11} + \sigma_{33}$
$\sqrt{6}\tau_5 = (-\sin^2\varphi + \sin\varphi\cos\varphi)\sigma_{11} + \sigma_{33}$
$\sqrt{6}\tau_6 = \sigma_{11}\cos 2\varphi$
$\sqrt{6}\tau_7 = (-\sin^2\varphi + \sin\varphi\cos\varphi)\sigma_{11} + \sigma_{33}$
$\sqrt{6}\tau_8 = -\sigma_{11}\cos 2\varphi$
$\sqrt{6}\tau_9 = (-\cos^2\varphi + \sin\varphi\cos\varphi)\sigma_{11} + \sigma_{33}$
$\sqrt{6}\tau_{10} = -\sigma_{11}\cos 2\varphi$
$\sqrt{6}\tau_{11} = (\cos^2\varphi + \sin\varphi\cos\varphi)\sigma_{11} - \sigma_{33}$
$\sqrt{6}\tau_{12} = (\sin^2\varphi + \sin\varphi\cos\varphi)\sigma_{11} - \sigma_{33}$

Table 6
Resolved shear stresses for the slip systems in the space $\sigma_{13}\sigma_{33}$

$\sqrt{6}\tau_1 = \sigma_{13}\sin\varphi + \sigma_{33}$
$\sqrt{6}\tau_2 = \sigma_{13}\cos\varphi + \sigma_{33}$
$\sqrt{6}\tau_3 = \sqrt{2}\sigma_{13}\sin(\varphi - \pi/4)$
$\sqrt{6}\tau_4 = -\sigma_{13}\sin\varphi + \sigma_{33}$
$\sqrt{6}\tau_5 = \sigma_{13}\cos\varphi + \sigma_{33}$
$\sqrt{6}\tau_6 = \sqrt{2}\sigma_{13}\cos(\varphi - \pi/4)$
$\sqrt{6}\tau_7 = -\sigma_{13}\cos\varphi + \sigma_{33}$
$\sqrt{6}\tau_3 = \sqrt{2}\sigma_{13}\cos(\varphi - \pi/4)$
$\sqrt{6}\tau_9 = \sigma_{13}\sin\varphi + \sigma_{33}$
$\sqrt{6}\tau_{10} = \sqrt{2}\sigma_{13}\cos(\varphi + \pi/4)$
$\sqrt{6}\tau_{11} = \sigma_{13}\sin\varphi - \sigma_{33}$
$\sqrt{6}\tau_{12} = \sigma_{13}\cos\varphi - \sigma_{33}$

$$\frac{\partial\rho}{\partial\varphi} = 0 \quad \text{hence } A'(\varphi)\cos\theta + B'(\varphi)\sin\theta = 0 \qquad (14)$$

This last equation is then substituted into Eq. (13), and different forms of yield surface functions are then obtained (smooth for $\boldsymbol{\sigma}^4$ and presenting corners for the other tensors). All the curves

Table 7
Resolved shear stresses for the slip systems in the space $\sigma_{12}\sigma_{11}$

$\sqrt{6}\tau_1 = (-\cos^2\varphi - \sin 2\varphi/2)\sigma_{11} + (\sin 2\varphi + \cos 2\varphi)\sigma_{12}$
$\sqrt{6}\tau_2 = (-\sin^2\varphi - \sin 2\varphi/2)\sigma_{11} - (\sin 2\varphi + \cos 2\varphi)\sigma_{12}$
$\sqrt{6}\tau_3 = -\sigma_{11}\cos 2\varphi + 2\sigma_{12}\sin 2\varphi$
$\sqrt{6}\tau_4 = (-\cos^2\varphi + \sin 2\varphi/2)\sigma_{11} + (\sin 2\varphi + \cos 2\varphi)\sigma_{12}$
$\sqrt{6}\tau_5 = (-\sin^2\varphi + \sin 2\varphi/2)\sigma_{11} - (\sin 2\varphi - \cos 2\varphi)\sigma_{12}$
$\sqrt{6}\tau_6 = \sigma_{11}\cos 2\varphi - 2\sigma_{12}\sin 2\varphi$
$\sqrt{6}\tau_7 = (-\sin^2\varphi + \sin 2\varphi/2)\sigma_{11} + (\cos 2\varphi - \sin 2\varphi)\sigma_{12}$
$\sqrt{6}\tau_8 = -\sigma_{11}\cos 2\varphi + 2\sigma_{12}\sin 2\varphi$
$\sqrt{6}\tau_9 = (-\cos^2\varphi + \sin 2\varphi/2)\sigma_{11} + (\sin 2\varphi + \cos 2\varphi)\sigma_{12}$
$\sqrt{6}\tau_{10} = -\sigma_{11}\cos 2\varphi + 2\sigma_{12}\sin 2\varphi$
$\sqrt{6}\tau_{11} = (\cos^2\varphi + \sin 2\varphi/2)\sigma_{11} - (\sin 2\varphi - \cos 2\varphi)\sigma_{12}$
$\sqrt{6}\tau_{12} = (\sin^2\varphi + \sin 2\varphi/2)\sigma_{11} + (\sin 2\varphi + \cos 2\varphi)\sigma_{12}$

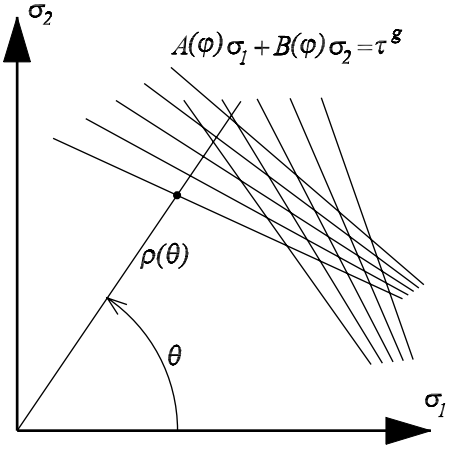

Fig. 6. Methodology used to calculate analytically yield surfaces of the static model.

(Fig. 7a–d) are plotted with a resolved shear stress $\tau^c = 100$ MPa.

For the stress tensor $\boldsymbol{\sigma}^1$, the yield surface is delimited by the six straight lines:

$$(\sqrt{2}+1)\sigma_{11} - (\sqrt{2}-1)\sigma_{22} = \pm 2\sqrt{6}\tau^c \qquad (15)$$

$$(\sqrt{2}-1)\sigma_{11} - (\sqrt{2}+1)\sigma_{22} = \pm 2\sqrt{6}\tau^c \qquad (16)$$

$$\sigma_{11} - \sigma_{22} = \pm\sqrt{6}\tau^c \qquad (17)$$

For the stress tensor $\boldsymbol{\sigma}^2$, the yield surface is delimited by the six straight lines:

$$-(\sqrt{2}+1)\sigma_{11} + 2\sigma_{33} = \pm 2\sqrt{6}\tau^c \qquad (18)$$

$$(\sqrt{2}-1)\sigma_{11} + 2\sigma_{33} = \pm 2\sqrt{6}\tau^c \qquad (19)$$

$$\sigma_{11} = \pm\sqrt{6}\tau^c \qquad (20)$$

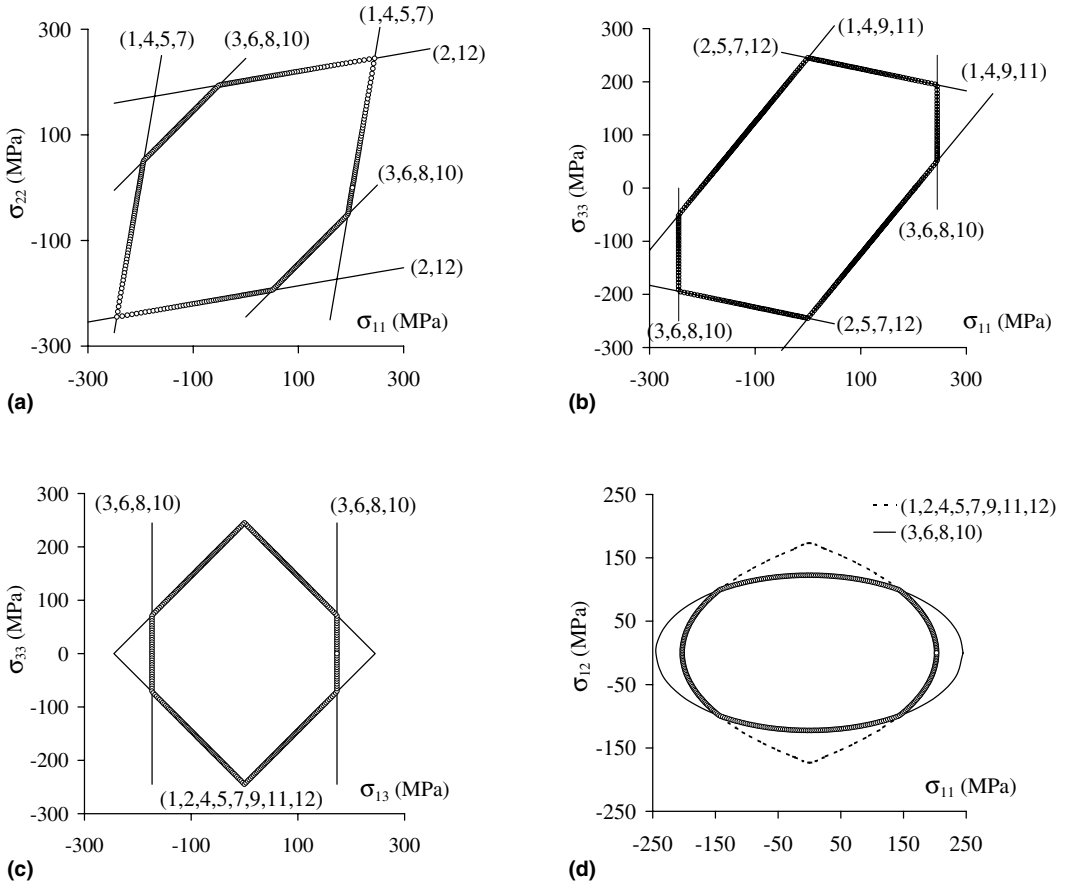

Fig. 7. Analytical yield surface for the static model: (a) space $\sigma_{11}\sigma_{22}$, (b) space $\sigma_{11}\sigma_{33}$, (c) space $\sigma_{13}\sigma_{33}$, (d) space $\sigma_{12}\sigma_{11}$.

For the stress tensor $\boldsymbol{\sigma}^3$, the yield surface is delimited by the six straight lines:

$$\sigma_{33} + \sigma_{13} = \pm\sqrt{6}\tau^c \tag{21}$$

$$\sigma_{33} - \sigma_{13} = \pm\sqrt{6}\tau^c \tag{22}$$

$$\sigma_{13} = \pm\sqrt{3}\tau^c \tag{23}$$

From Fig. 7c, one can easily show that the polygonal area inside the yield surface in space $\sigma_{13}\sigma_{33}$ is almost equal to $10.97\tau_c^2$. For the stress tensor $\boldsymbol{\sigma}^4$, the yield surface is delimited by the curves:

$$\rho = \frac{\pm 2\sqrt{6}\tau^c}{\cos\theta + \sqrt{2}\sqrt{1+3\sin^2\theta}} \tag{24}$$

$$\rho = \frac{\pm\sqrt{6}\tau^c}{\sqrt{1+3\sin^2\theta}} \tag{25}$$

with

$$\sigma_{11} = \rho\cos\theta \quad \text{and} \quad \sigma_{12} = \rho\sin\theta \tag{26}$$

It can be shown that the intersection of the two last curves is obtained for an angle $\theta_i = \mathrm{Arcsin}\sqrt{(4\sqrt{2}-5)/(19-12\sqrt{2})}$ which is approximatively equal to 35°. Note that this value is independent of the critical resolved shear stress. Accordingly, the value of the area inside the yield surface in space $\sigma_{11}\sigma_{12}$ can be calculated by integration of two domains from 0 to θ_i and from θ_i to $\frac{\pi}{2}$. This area is almost equal to $8.15\tau_c^2$. Hence, the area inside the yield surface in space an $\sigma_{11}\sigma_{12}$ is smaller then the area inside the yield surface in space $\sigma_{13}\sigma_{33}$. Indeed, the equivalent stress in space $\sigma_{11}\sigma_{12}$ is always perpendicular to the $\langle 0\,0\,1\rangle$ axes. As a result, the possibility of finding an active system is larger than in the space $\sigma_{13}\sigma_{33}$.

4.3. Comparison with FE model

The aim of this section is to assess the quality of the static model. The polycrystalline model using the simplest transition rule of Section 4.1 (uniform stress assumption, Eq. (8)) is considered. This corresponds to a representative volume element (RVE) computation in which the aggregate is selected so that the orientation distribution is the same as in FE-64-64. The same tensile and shear tests are performed with the static model and then compared to the FE-64-64 responses. Fig. 8a shows no difference for tensile test in 33 direction, whereas small differences are observed for 11 and 22 directions. However, a significant deviation is observed for shear test (Fig. 8b), especially for 12 test, meanwhile either 12 and 13 shear levels are underestimated by the static model. This discrepancy is just a remainder that a model must be checked for all types of loadings, and demonstrates that using a super single crystal approach is not a valid assumption for a general purpose DS material model. It is then necessary to introduce an appropriate transition rule in an improved model. This is the subject of the following section.

5. The β-model

In the previous section, it was shown that the static assumption may fail to describe correctly the DS behavior. This is mainly due to the presence of non-uniform stresses in the different grains in the case of shear test and tensile tests in directions 11 and 22. The material presenting a random character in the plane normal to x_3, the self-consistent scheme is a good candidate to represent the intergranular interaction. Instead of using the full self-consistent formalism, what is presented here is an explicit transition rule, which requires no integral differential equation to be solved for characterizing the scale transition. The model involves a set of parameters (only one for isotropic behavior) that can be calibrated before use by means of FE computations on representative cells.

5.1. Constitutive equations

The initial idea of the model is to start from Kröner's approach of the elastic accommodation problem which uses Eshelby's solution (Eshelby, 1957) for an ellipsoidal inclusion in an infinite medium. The corrective term proposed by Kröner to compute the local stresses is the product of a fourth order tensor by the difference between average strain and local strain (Eq. (27)). The fourth order tensor involves the elastic moduli tensor $\boldsymbol{C}$, the fourth order unit tensor $\boldsymbol{I}$ and Eshelby's tensor $\boldsymbol{S}$ (Sanchez-Palencia and Zaoui, 1987). In the present model (Eq. (28)), these tensors are still used, but the local strain is replaced by a phenomenological variable $\boldsymbol{\beta}^g$, that presents a nonlinear evolution with respect to plastic strain (Eq. (29)). Replacing total strain by $\underset{\sim}{\beta}$ assumes that the main source of

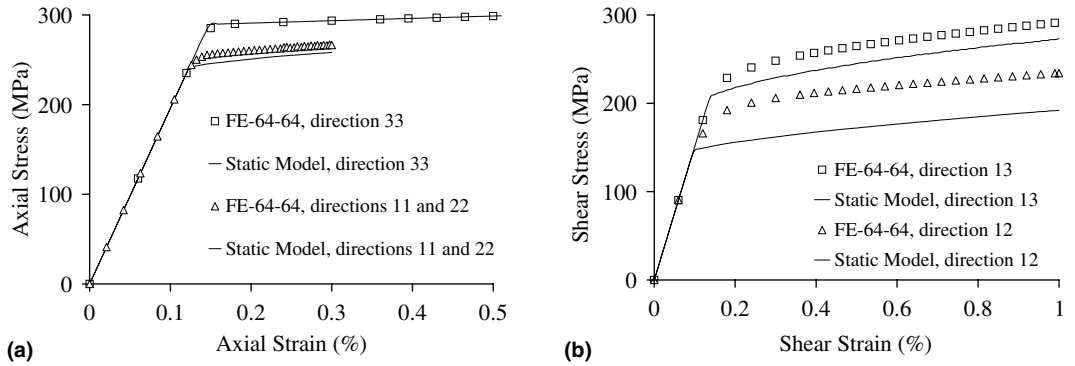

Fig. 8. Fitting on uniaxial strain controlled test. Comparison between the static model and the aggregate FE-64-64 model: (a) tensile tests, (b) shear tests.

heterogeneity is plasticity more than elasticity. This new variable was shown able to correctly capture the plastic accommodation which comes from the self-consistent formalism (Cailletaud, 1987; Cailletaud and Pilvin, 1994; Pilvin, 1996).

$$\boldsymbol{\sigma}^{g} = \boldsymbol{\sigma} + \boldsymbol{C} : [(\boldsymbol{I} - \boldsymbol{S}) : (\boldsymbol{\varepsilon} - \boldsymbol{\varepsilon}^{g})] \tag{27}$$

$$\boldsymbol{\sigma}^{g} = \boldsymbol{\sigma} + \boldsymbol{C} : [(\boldsymbol{I} - \boldsymbol{S}) : (\boldsymbol{\beta} - \boldsymbol{\beta}^{g})] \tag{28}$$

$$\dot{\boldsymbol{\beta}}^{g} = \dot{\boldsymbol{\varepsilon}}^{pg} - \boldsymbol{D} : \boldsymbol{\beta}^{g} \sum_{s \in g} |\dot{\gamma}^{s}| \tag{29}$$

Since the grains are elongated in one direction, the chosen $\boldsymbol{S}$ tensor is Eshelby's tensor for a cylindrical inclusion, obtained from the elliptic solution by assuming that two dimensions are equal ($a_1 = a_2$) and that the third one tends to infinity ($a_3 \to \infty$) (Mura, 1987).

In the material axes, the tensor $\boldsymbol{D}$ has the following form, with six independent material parameters:

$$\boldsymbol{D} = \begin{pmatrix} D_{11} & D_{12} & D_{23} & 0 & 0 & 0 \\ D_{12} & D_{11} & D_{23} & 0 & 0 & 0 \\ D_{23} & D_{23} & D_{23} & 0 & 0 & 0 \\ 0 & 0 & 0 & D_{44} & 0 & 0 \\ 0 & 0 & 0 & 0 & D_{55} & 0 \\ 0 & 0 & 0 & 0 & 0 & D_{55} \end{pmatrix} \tag{30}$$

Using the deviatoric property of the accommodation variable trace $\dot{\boldsymbol{\beta}}^{g} = 0$ the following additional condition is enforced:

$$D_{33} = D_{11} + D_{12} - D_{23} \tag{31}$$

On the other hand, the form of $\boldsymbol{S}$ is the following:

$$\boldsymbol{S} = \begin{pmatrix} S_{1111} & S_{1122} & S_{1133} & 0 & 0 & 0 \\ S_{2211} & S_{2222} & S_{2233} & 0 & 0 & 0 \\ 0 & 0 & 0 & 0 & 0 & 0 \\ 0 & 0 & 0 & S_{1212} & 0 & 0 \\ 0 & 0 & 0 & 0 & S_{1313} & 0 \\ 0 & 0 & 0 & 0 & 0 & S_{2323} \end{pmatrix} \tag{32}$$

This Eshelby tensor $\boldsymbol{S}$ corresponds to the plane strain hypothesis. This must be complemented by the following condition which is enforced for each crystal orientation:

$$\varepsilon_{33}^{g} = \varepsilon_{33} \tag{33}$$

After some algebraic manipulations, a condition between the components of the local and global stress tensors is derived:

$$\sigma_{33}^{g} = \sigma_{33} + \nu(\sigma_{11}^{g} - \sigma_{11}) + (\sigma_{22}^{g} - \sigma_{22}) \tag{34}$$

5.2. β-model–FE identification

The FE-64-64 computation is taken as a reference to calibrate the scale transition rule of the β-model. The material parameters describing crystal behavior are the same in both computations

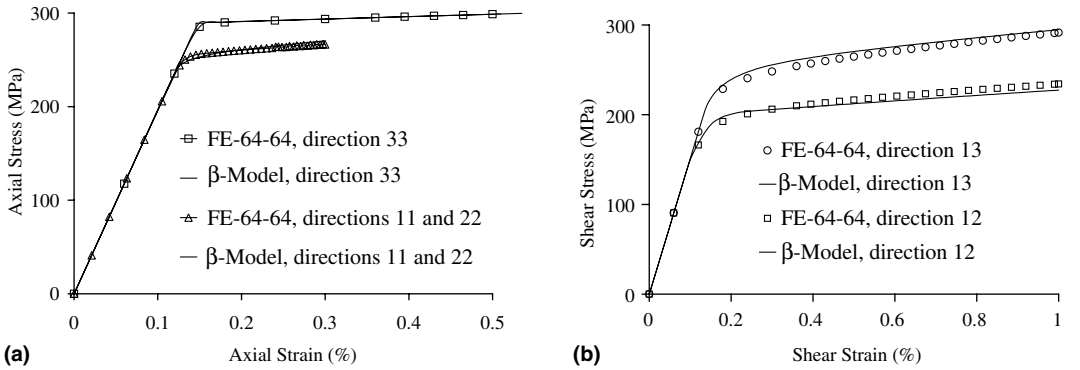

Fig. 9. Fitting on uniaxial strain controlled test. Comparison between the β-model and the aggregate FE-64-64 model: (a) tensile tests, (b) shear tests.

(FE and β-model). The only parameters to determine are those introduced in the matrix $\boldsymbol{D}$ defined in Eq. (30). The global response of the RVE described by FE-64-64 is computed by averaging the stress and strain component on the whole mesh. The database generated with FE computations includes tensile tests (Fig. 9a) and shear tests (Fig. 9b). The scale transition parameters in matrix $\boldsymbol{D}$ are identified by comparing the loading curves coming from FE and β-model integration. As shown by the figures, the responses obtained with the two approaches are in good agreement with the chosen set of coefficients ($D_{11} = 1000$, $D_{12} = 75$, $D_{23} = 100$, $D_{44} = 10$, $D_{55} = 100$).

5.3. Model validation

Fig. 8a shows a comparison between the β-model and the FE-64-64 aggregate model for a biaxial test not included in the database of the identification procedure. The two models are in good agreement. On the other hand, the β-model can be used in principle for non-monotonic loading conditions. It is then necessary to compare its response for a cyclic loading and that of the FE aggregate model. Fig. 8b shows the comparison for a test in which a symmetric shear strain is imposed. This test was not included in the identification procedure and is thus a validation of the model. This remarkable agreement shows the kinematic character of intergranular stresses (Fig. 10).

After having validated the β-model on a macroscale, it is necessary to assess its reliability at the grain level (level 2). Note that a different strategy would consist in solving the inverse problem made of the global response and the local responses taken together to identify the material parameters. The present approach is more simple, and is proved to provide an acceptable solution. Two orientations are selected for that purpose $\varphi = 20°$ and $\varphi = 50°$. Fig. 11a–c show that the β-model is in good agreement with FE calculations for tensile tests as well as for shear tests.

An other mean to make the assessment at the microscopic level, for a given macroscopic strain level, is to compare the mean stress per orientation predicted by the β-model and the FE calculation. In Fig. 11d the X-coordinate of a given point

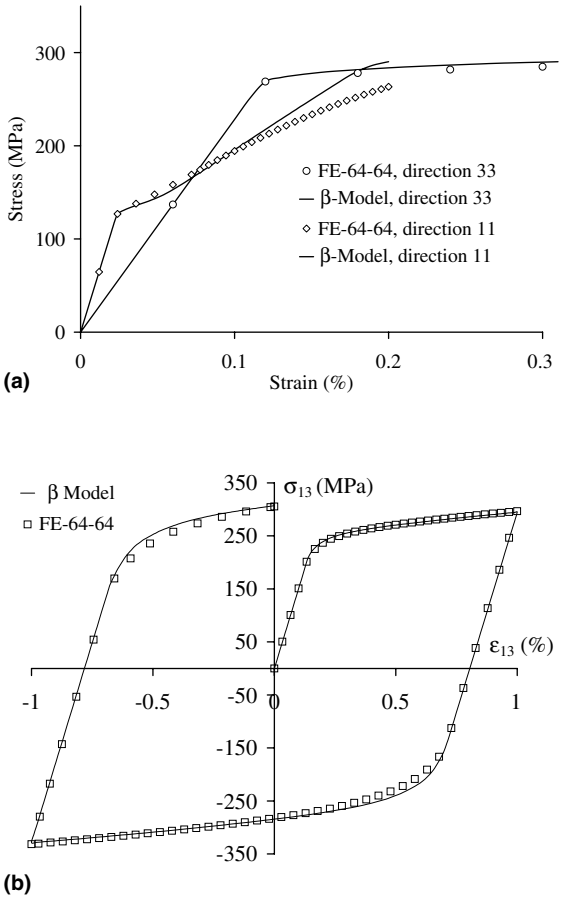

Fig. 10. Validation of the identification procedure: comparison between the β-model and the aggregate FE-64-64 model: (a) tensile biaxial test, (b) shear strain controlled cyclic loading.

(corresponding to a given orientation) is the local stress obtained by the β-model whereas the Y-coordinate is the local stress given by the FE simulation. It can be seen that the group of points is close to the first bissectrice.

5.4. Intergranular heterogeneity

Fig. 12a shows for two selected orientation, $\varphi = 20°$ and $\varphi = 60°$, the influence of the location of the grain. It can be seen that these variations are weak. So that global and local responses of FE-64-64 simulations and FE-64-8 simulations are almost identical.

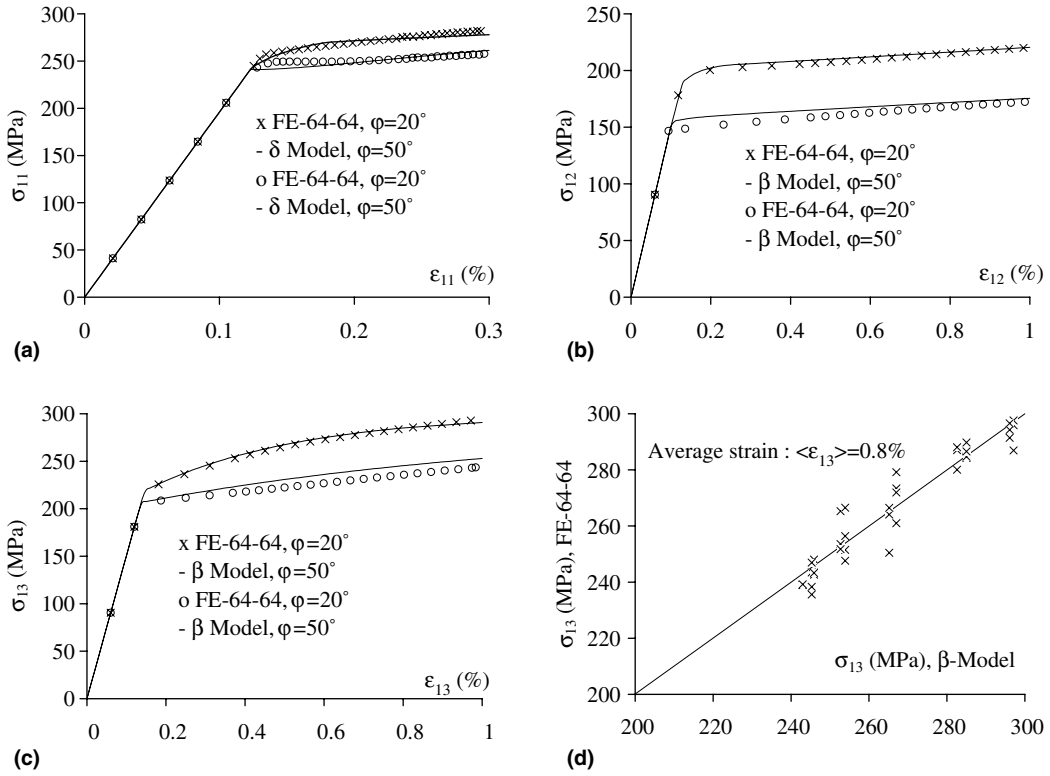

Fig. 11. Comparison between the β-model and the FE aggregate model, local stress–strain curves in uniaxial strain controlled tests: (a) tensile test 11, (b) shear test 12, (c) shear test 13, (d) local shear stress in uniaxial strain controlled shear test 13. β-model vs FE-64-64 model.

After checking the response of the β-model on macroscopic model on both macroscopic and microscopic stress–strain curves, it is also important to evaluate the quality of the transition rule with respect to intergranular heterogeneity. This is made by comparing the average response of the elements having the same orientation in the FE computation with the corresponding local response for the same crystallographic phase in the β-model. Note that due to the additional condition (34) the intergranular strain heterogeneities vanish for the 33 direction. The heterogeneities are more significant for shear tests than for tensile tests (Fig. 12b–d). Furthermore, in the yield surfaces presented in Section 4.2 it was shown that when the stress components are contained in a plane perpendicular to the $\langle 001 \rangle$ axes, there is a large amount of relative orientations between the crystals and the loading frame. This is why the 12 shear test exhibits a more significant intergranular heterogeneity than 13 shear test.

6. Conclusions

The purpose of the paper was to test the capabilities of a micro-mechanical mean field model to represent mechanical behaviour of DS materials. A FE model in which grains are represented by a group of elements with columnar morphology is used to generate a material database. A number of loading cases are considered to account for the orthotropic character of the resulting unit cell. The results of the FE computations provide information at three levels:

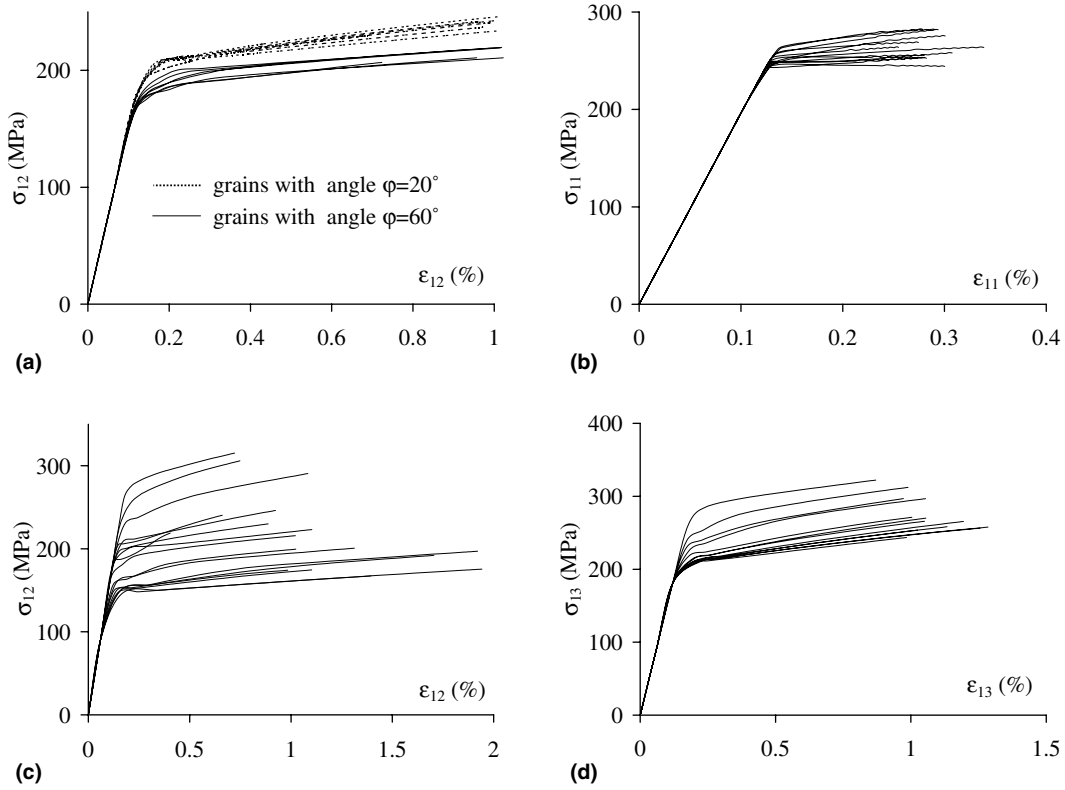

Fig. 12. (a) FE study of the influence of the location of the grain (FE-64-8). Uniaxial strain controlled shear test 12. Intergranular heterogeneity in β-model. (b) Strain controlled tensile test 11. (c) Strain controlled shear test 12. (d) Strain controlled shear test 13.

- Macroscopic level, using the volume average over all Gauss points.
- Phase scale, using the volume average over the Gauss points of the elements having the same orientation.
- Intragranular level, which concerns the individual Gauss points.

An attempt is first made with a static model, but it is demonstrated that such an approach gives satisfactory results only for a tension along the growth axis, and fails to represent any type of shear loading. A transition rule is then necessary to account for residual stresses on the phase level. A β-rule is used for that purpose. It is successfully calibrated on the whole numerical data base, using the macroscopic responses. A detailed analysis is then shown, in order to evaluate the scatter to be expected on the other scales. The β-rule correctly represents the stress and strain range on the level of the phase. Further developments have to be made to capture an evaluation of the intragranular scatter.

It is worth noting that this good prediction capability can be obtained without capturing the intragranular heterogeneities. This has to be related to the fact that the global response is the result of a series of averages, which are acceptable with the present microstructure (texture and slip system). It does not demonstrate that the result is general, nevertheless, it has already be validated in similar conditions on a FCC aggregate (Barbe et al., 2001). The β-model is implemented in the FE element code Zebulon (Besson et al., 1998). In the present state, it is possible to use the β-model as the constitutive equations in the FE method to analyse inelastic behaviours of machine components made of DS material submitted to multiaxial thermomechanical loadings.

References

Barbe, F., Forest, S., Cailletaud, G., 2001. Intergranular and intragranular behavior of polycrystalline aggregates. Part II: Results. Int. J. Plast. 17 (4), 537–566.

Besson, J., Leriche, R., Foerch, R., Cailletaud, G., 1998. Object-oriented programming applied to the finite element method. Part II. Application to material behaviors. Rev. Eur. Eléments Finis 7, 567–588.

Cailletaud, G., 1987. Une approche micromécanique phénoménologique du comportement inélastique des métaux. Ph.D. thesis, Université Pierre et Marie Curie, Paris 6.

Cailletaud, G., Forest, S., Jeulin, D., Feyel, F., Galliet, I., Mounoury, V., Quilici, S., 2003. Some elements of microstructural mechanics. Comput. Mater. Sci. 27, 351–374.

Cailletaud, G., Pilvin, P., 1994. Utilisation de modéles polycristallins pour le calcul par éléments finis. Rev. Eur. Eléments Finis 3, 515–541.

Eshelby, J., 1957. The determination of the elastic field of an ellipsoidal inclusion and related problems. Proc. Roy. Soc. London A 241, 376–396.

Gilbert, E., 1962. Random subdivisions of space into crystals. Ann. Math. Stat. 33.

Hill, R., 1965. Continuum micro-mechanisms of elastoplastic polycrystals. J. Mech. Phys. Solids 13, 89–101.

Méric, L., Poubanne, P., Cailletaud, G., 1991. Single crystal modeling for structural calculations. Part 1: Model presentation. J. Eng. Mater. Technol. 113, 162–170.

Molinari, A., 1999. Extensions of the self-consistent tangent model. Model. Simul. Mater. Sci. Eng. 7, 683–697.

Mura, T., 1987. Micromechanics of defects in solids. second revised ed.

Pilvin, P., 1996. The contribution of micromechanical approaches to the modelling of inelastic behaviour of polycrystals. In: André, P., Georges, C., Trevor, L. (Eds.), Fourth Int. Conf. on Biaxial/Multiaxial Fatigue and Design, ESIS, 21. Mechanical Engineering Publications, London.

Sanchez-Palencia, E., Zaoui, A., 1987. Homogenization techniques for composite media. Lecture Notes in Physics, vol. 272. Springer, Berlin.

Sarma, G.B., Dawson, P., 1995. Effects of interactions among crystals on the inhomogeneous deformations of polycrystals. Acta Mater. 44, 1937–1953.

Taylor, G., 1938. Plastic strain in metals. J. Inst. Metals 62, 307–324.

Yaguchi, M., Busso, E., 2005. On the accuracy of self-consistent elasticity formulations for directionally solidified polycrystal aggregates. Int. J. Solids Struct. 42 (3–4), 1073–1089.